# scientific reports

OPEN

# Enhancement of magnetization and optical properties of CuFe$_2$O$_4$/ZnFe$_2$O$_4$ core/shell nanostructure

A. M. Faramawy$^{\boxtimes}$ & H. M. El-Sayed

In this work, core/shell of CuFe$_2$O$_4$/ZnFe$_2$O$_4$ nanostructure composite was prepared by hydrothermal method. X-ray diffraction (XRD) analysis, transmission electron microscope imaging, energy dispersive X-ray (EDX), and Fourier transform infrared techniques were used to prove the phase formation, morphology, elemental analysis, and cation distribution of core/shell structure, respectively. Furthermore, measurement of the optical properties proved the decrease of photoluminescence (PL) efficiency. The magnetic measurements showed an enhancement of the magnetization by about 63% relative to pure Cu ferrite, and the magnetization curve exhibited superparamagnetic behavior. These results were explained in terms of the depression of the magnetic dead layer thickness in the core/shell structure. The results unleash the promising applications of the prepared samples as transformer cores in the high frequency range and as a photocatalytic agent for water purification and hydrogen production.

Nano ferrites (NFs) have been regarded as crucial materials for modern technologies in the last 20 years. The study of the chemical and physical properties of nano-ferrite (NF) materials is intricate because of the impact of miniaturizing the structure on the magnetic, electric, and optical features that these materials possess[1,2]. In addition, the dopant ions, chemical composition, synthesis procedures, thermal treatments, and shape play a crucial role in determining their characteristics. Applications of NFs include medical, telecommunications, wave absorbers, data recording, chemical sensors, microwave devices, sustainable sources, giant magnetoresistive devices (GMR), magnetic resonance imaging (MRI) technology, drug delivery systems, etc[2-7].

Intense research is currently in progress on the synthesis and application of magnetic nanoparticles core/shell composites. These important materials have been synthesized and investigated by several research groups during the last few years. There are many reviews in the literature about core/shell ferrite nanoparticles, discussing their different synthesis conditions and techniques[8-11] and the obtained properties including magnetic[12], magneto-electric[13] and optical properties[13]. Their applications in drug delivery[13], water remediation, and catalysis[14,15] are also subject to intense research. Zinc ferrite (ZnFe$_2$O$_4$) is used as semiconductor photo-catalyst for various processes, due to its ability to absorb visible light and its high efficiency, which shows potentially wide applications in photoinduced transformer, photoelectrochemical cells and photochemical hydrogen production[16-20]. Moreover, ZnFe$_2$O$_4$ as a core and ZnO as a shell were investigated by Rong Shao et al. for photocatalysis and was prepared via solvothermal method[21]. The photocatalytic activity of the novel ZnFe$_2$O$_4$/ZnO sample was higher than that of pure ZnO and the highest photocatalytic activity was observed in samples prepared with a 1:10 molar ratio of ZnFe$_2$O$_4$ to ZnO. ZnFe$_2$O$_4$/SiO$_2$/TiO$_2$ nanoparticles as magnetic photocatalysts for etodolac degradation was studied by Eryka Mrotek et al.[14]. The coupling between Zn ferrite and oxide materials significantly enhanced etodolac breakdown and mineralization as evaluated by TOC removal. As an alternative to more often utilized metal oxides, spinel copper ferrite (CuFe$_2$O$_4$) has recently been used for very wide range of applications as a photoanode for water oxidation, photocathodes for hydrogen evolution, photocatalyst and sensor due to its narrow band gap (1.54–1.9 eV)[22,23]. Thu Uyen Tran Thi et al.[24] synthesized CuFe$_2$O$_4$/Fe$_2$O$_3$ core/shell to study the effective photo-Fenton-like catalysts for the methylene blue degradation process using oxalic acid as a radical generator. It was noticed that catalytic performance was two times greater than that of the CuFe$_2$O$_4$ sample in a 1:2 CuFe$_2$O$_4$/Fe$_2$O$_3$, with a rate constant of 2.103 h$^{-1}$ when exposed to UVA light and 0.542 h$^{-1}$ when exposed to visible light. Using laser Raman spectroscopy, Balaji et al.[25] examined the formation of CuFe$_2$O$_4$-polyaniline

Department of Physics, Faculty of Science, Ain Shams University, Abbassia 11566, Cairo, Egypt. $^{\boxtimes}$email: ahmed_faramawy@sci.asu.edu.eg

core/shell nanocomposites prepared by in situ polymerization method. Shuo-Hsiu Kuo et al.[26] fabricated Cu ferrite-polymer as core/shell nanoparticles to study cervical cancer cell photodynamic ablation. It was found that the superparamagnetic characteristics of Cu ferrite-polymer are promising MRI contrast agents and may be utilized as a Fenton catalyst to transform $H_2O_2$ into ROS.

Thus, based on the above survey, there are very few reports on the properties of $CuFe_2O_4/ZnFe_2O_4$ core/shell. Herein, hydrothermal technique was used to prepare bare $ZnFe_2O_4$ and $CuFe_2O_4$ nanoparticles, as well as $CuFe_2O_4/ZnFe_2O_4$ core/shell nanoparticles for studying the structural, optical, and magnetic properties of these three samples.
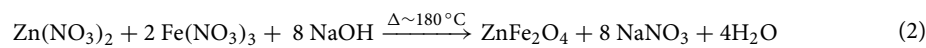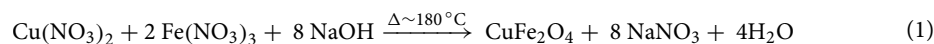
## Materials and methods
### Materials
The iron (III) nitrate nonahydrate ($Fe(NO_3)_3.9H_2O$) (99.99%, Alfa Aesar), copper (II) nitrate hexahydrate ($Cu(NO_3)_2.6H_2O$) (99.5% LOBA Chemie), zinc (II) nitrate hexahydrate ($Zn(NO_3)_2.6H_2O$) (98% LOBA Chemie), and sodium hydroxide (NaOH) purchased from Sigma Aldrich utilized in the preparation of the pure and core/shell nano-ferrites were all of analytical grade, and deionized water was used as the solvent.

### Synthesis of copper and zinc ferrites by the hydrothermal method
Copper ferrite nanoparticles were synthesized through the dissolution of ($Cu(NO_3)_2 \cdot 6H_2O$), and ($Fe(NO_3)_3 \cdot 9H_2O$) by molar ratio 1:2 in deionized water. The pH of the precursor solution was adjusted to a value of 10 by drop-wise addition of a sodium hydroxide (NaOH) solution while vigorously stirring. After being stirred continuously for one hour, the solution was transferred into a 100 mL Teflon-lined stainless-steel autoclave. The autoclave was subjected to a thermal treatment at a temperature of 180 °C for 18 h. Following the completion of the hydrothermal reaction, the autoclave was subsequently removed from the reaction environment and allowed to cool to ambient temperature. The same process was employed for the preparation of zinc ferrite nanoparticles. The resulting product of both $CuFe_2O_4$ and $ZnFe_2O_4$ was subjected to filtration and subsequent washing with water, repeated multiple times until the pH reached a value of 7.0. After drying at 95 °C for 3 h, the $CuFe_2O_4$ powder was divided into two portions. The first portion was used as bare $CuFe_2O_4$, and the other portion served as the core for the core/shell composite sample. The chemical reaction for the preparation of both copper ferrite ($CoFe_2O_4$) and zinc ferrite ($ZnFe_2O_4$) nanoparticles is as follows:

$$Cu(NO_3)_2 + 2\,Fe(NO_3)_3 + 8\,NaOH \xrightarrow{\Delta\sim180\,°C} CuFe_2O_4 + 8\,NaNO_3 + 4H_2O \tag{1}$$

$$Zn(NO_3)_2 + 2\,Fe(NO_3)_3 + 8\,NaOH \xrightarrow{\Delta\sim180\,°C} ZnFe_2O_4 + 8\,NaNO_3 + 4H_2O \tag{2}$$

### Synthesis of the $CuFe_2O_4/ZnFe_2O_4$ core/shell magnetic nanocomposite
To coat the surface of the prepared $CuFe_2O_4$ (core) with $ZnFe_2O_4$ (as shell), 1 gm of $CuFe_2O_4$ nanoparticles was transferred to the autoclave along with the precursors for the synthesis of $ZnFe_2O_4$. The mass ratio between $ZnFe_2O_4$ to $CuFe_2O_4$ is 2:1. Here, $CuFe_2O_4$ nanoparticles serve as seeds for the crystal growth of $ZnFe_2O_4$ because of the good lattice matching between the core and the shell. The resulting product was subjected to filtration and subsequently washed multiple times with water until the pH of the solution reached 7.0. Finally, the core/shell sample was dried at 95 °C for 3 h. Figure 1 illustrates a schematic diagram for the synthesis of the core/shell composite samples by hydrothermal method.

### Samples characterizations
X-ray diffraction (XRD; BrukerAXSD8Advance, Bruker, Germany) was used to characterize the samples. For studying the microstructure and estimating the particle size, a transmission electron microscope (henceforth, TEM) (Jeol–Jem 1230 electron microscope) was used. Energy Dispersive X-ray (EDX) measurements were carried out using a TESCAN VEGA COMPACT SEM with Tungsten filament as an electron source and an attached EDX detector (Czech Republic). Fourier transform infrared spectroscopy (FTIR) was performed at room temperature in transmission mode (Spectrometer JASCO, 6300, Japan)) in the range of 400–4000 cm$^{-1}$. Room temperature photoluminescence (PL) spectra with an excitation wavelength of 325 nm were obtained using a (FLUOROMAX-2 spectrofluorometer, JOBIN YVON—SPEX, New Jersey; USA). A room-temperature vibrating sample magnetometer (VSM) (model Lake Shore no. 7410 US) was used to measure the magnetic properties in a field up to 20 kG. Finally, the assessment of the AC loss of the samples when exposed to an AC magnetic field with a frequency of 66.5 kHz and a magnetic field strength of 1.45 kAm$^{-1}$; was conducted by measuring the increase in temperature over time.

## Results
### X-ray diffraction (XRD) analysis
Figure 2 shows the X-ray diffraction patterns of Cu ferrite ($CuFe_2O_4$), Zn ferrite ($ZnFe_2O_4$), and $CuFe_2O_4/ZnFe_2O_4$ core/shell samples. All of the reflection peaks match well with the typical JCPDS cards No. 34-0425[27] and 22-1012[28] of pure $CuFe_2O_4$ and $ZnFe_2O_4$ phases, respectively, with no external peaks indicating that all the produced samples crystallized as a single-phase cubic structure with Fd-3m space group[29]. On the other hand, a small phase percentage of the hematite (α-$Fe_2O_3$) in the core/shell sample was obtained[5,30]. Furthermore, all samples were subjected to Rietveld analysis using the MAUD software programme[31] in order to accurately characterize the crystal structure and determine the lattice constant ($a_{fit}$.) and crystallite size ($L_{fit}$.). Figure 3
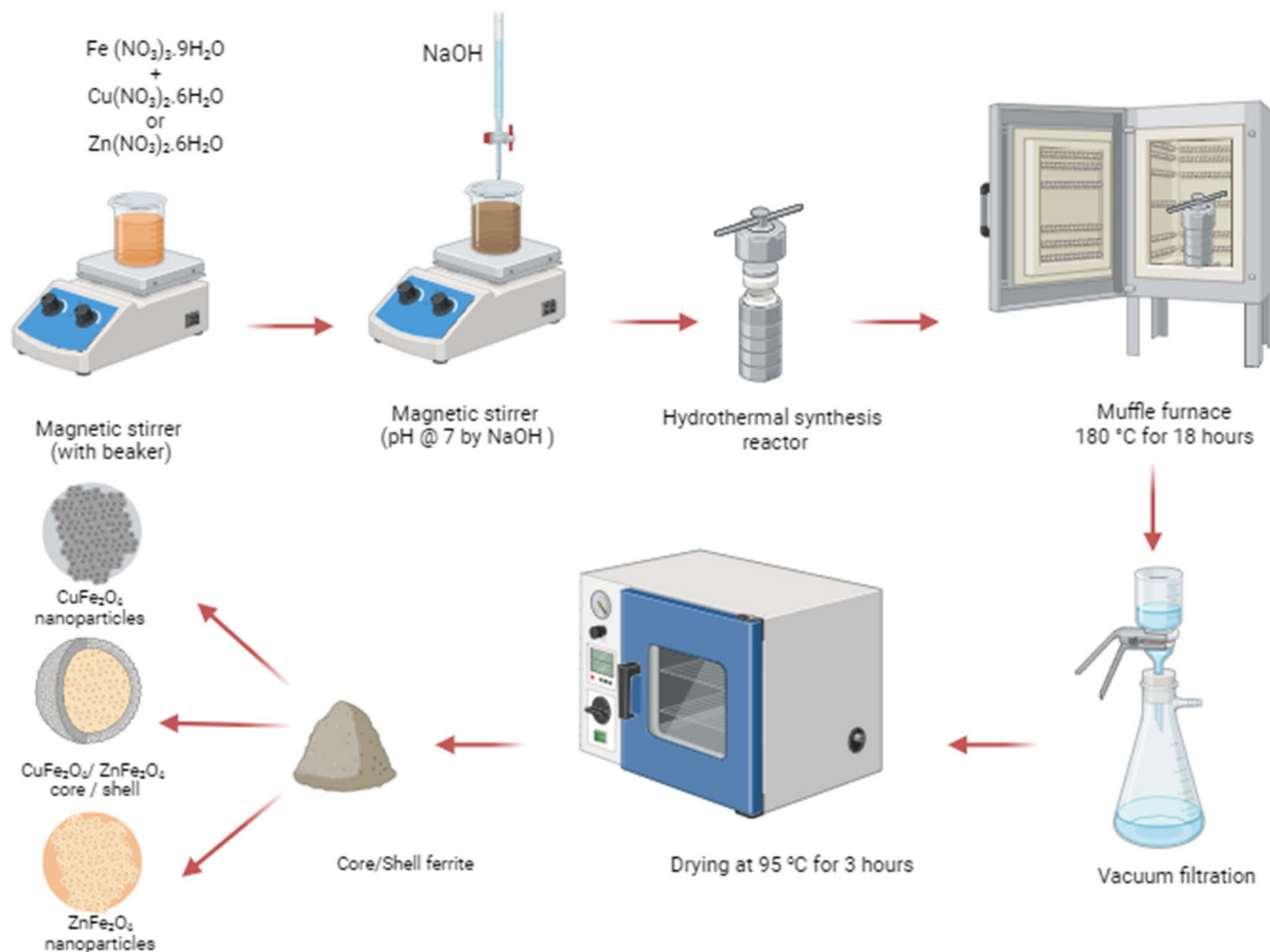
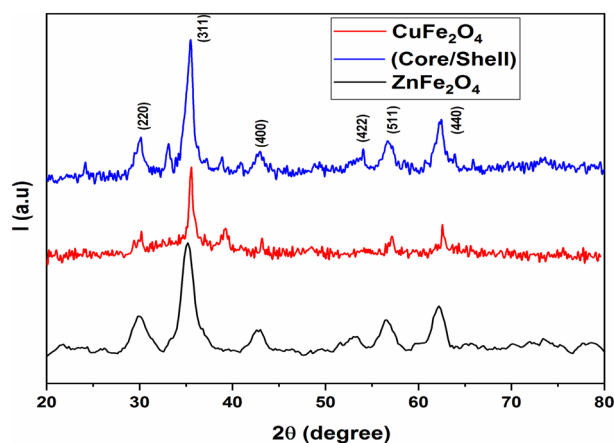**Figure 1.** Schematic diagram for the synthesis of the core/shell composite samples by hydrothermal method.



**Figure 2.** XRD patterns of CuFe$_2$O$_4$, ZnFe$_2$O$_4$ and CuFe$_2$O$_4$/ZnFe$_2$O$_4$ core/shell samples.

illustrates the outcomes of the fitted profile. The process of refinement was carried out iteratively until reaching convergence with a goodness factor approaching one, approximately[2,29]. Table 1 includes both the ($a_{fit.}$) and ($L_{fit.}$) values with the corresponding refinement standard deviation parameter for the investigated samples. It was found from refinement fitting that the phase percentages of ZnFe$_2$O$_4$, CuFe$_2$O$_4$, and hematite (α-Fe$_2$O$_3$) are (82.25%), (2.33%) and (15.42%), respectively. Such a result confirms that the CuFe$_2$O$_4$ was covered by ZnFe$_2$O$_4$. The calculated lattice constant ($a_{cal.}$) for the three samples was computed using the following relation:
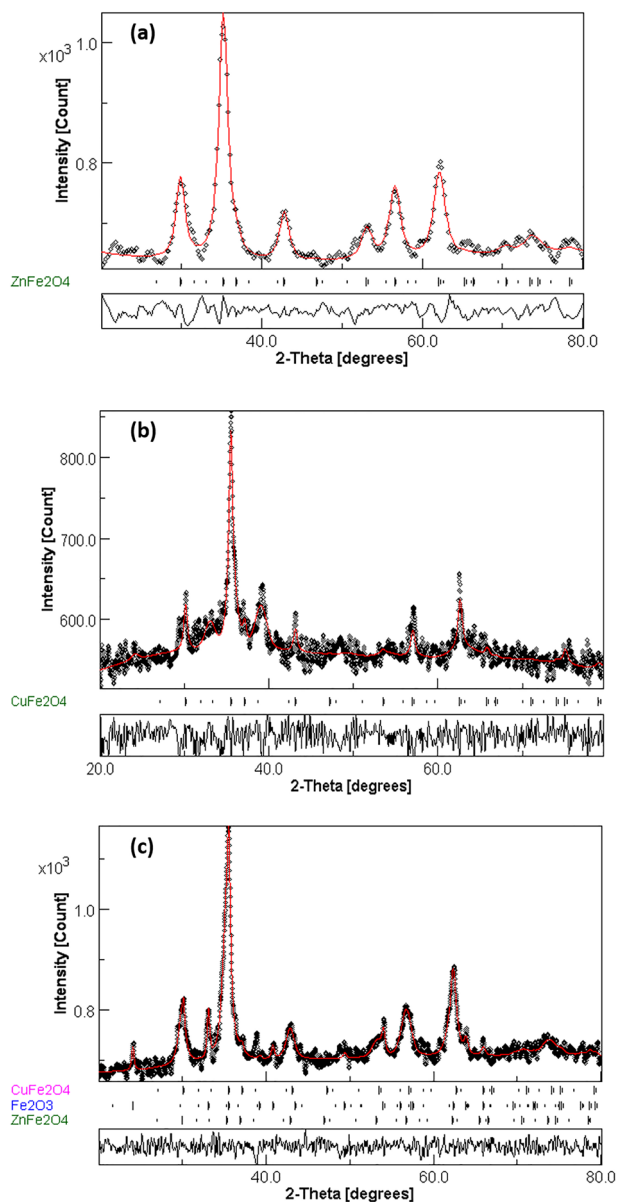
**Figure 3.** Rietveld refinement profile for (**a**) ZnFe$_2$O$_4$, (**b**) CuFe$_2$O$_4$, and (**c**) CuFe$_2$O$_4$/ZnFe$_2$O$_4$ core/shell nanoparticles using MAUD program.

| Sample | FWHM | $a_{cal.}$(Å) | $a_{fit.}$(Å) | $L_{cal.}$(nm) | $L_{fit.}$(nm) | D (nm) | σ | ε | M$_s$ (emu/g) |
|--------|------|--------------|--------------|---------------|---------------|--------|------|--------|--------------|
| CuFe$_2$O$_4$ | 1.084 | 8.388 | 8.398 | 8.79 | 8.21 | 9 | 0.441 | 0.0029 | 7.6 |
| ZnFe$_2$O$_4$ | 1.395 | 8.437 | 8.440 | 10.56 | 9.63 | 12 | 0.390 | 0.0005 | 10 |
| Core/Shell | 0.601 | 8.418 | 8.419 | 19.91 | 15.79 | 25 | 0.372 | 0.0033 | 12.4 |

**Table 1.** Compositions, full width at half-maximum (FWHM), lattice parameter ($a_{cal.}$ and $a_{fit.}$), crystallite size ($L_{cal.}$ and $L_{fit}$) estimated from XRD, particle size (D) estimated from TEM, refinement standard deviation parameter (σ), strain (**ε**) and magnetization (M$_s$) of investigated samples.

$$\frac{1}{d_{hkl}^2} = \frac{\left(h^2 + k^2 + l^2\right)}{a^2} \tag{3}$$

where $d_{hkl}$ denotes the inter-planar spacing in the XRD pattern and (hkl) are the Miller indices of the main peaks. In addition, the Williamson-Hall (W–H) Eq.[32] is used to obtain the calculated average crystallite size ($L_{cal.}$) as well as the micro strain (ε) for the three samples. The calculated values of ($a_{cal.}$) and ($L_{cal.}$) are also given in Table 1. One can see that, the lattice parameter values for $CuFe_2O_4$ and $ZnFe_2O_4$ are consistent with those reported in[18,20,27]. In addition to this, the lattice parameter of $CuFe_2O_4$/$ZnFe_2O_4$ core/shell is quite similar to that of pure $ZnFe_2O_4$. The lattice matching between $ZnFe_2O_4$ and $CuFe_2O_4$ causes $ZnFe_2O_4$ crystals to grow as a shell on $CuFe_2O_4$ as a seed[33].

In addition, when considering the crystallite size of $CuFe_2O_4$/$ZnFe_2O_4$ in comparison to both bare ferrites; it becomes evident that the crystallite size of the core/shell sample is greater than that of bare $ZnFe_2O_4$ and $CuFe_2O_4$ by approximately 9 nm. This observation provides evidence for the formation of core/shell nanoparticles. Furthermore, it can be observed that the lattice strain—Table 1—in the $CuFe_2O_4$/$ZnFe_2O_4$ core/shell is higher compared to that of the pure $CuFe_2O_4$. This increase in lattice strain can be attributed to the minimal difference in lattice parameters between $ZnFe_2O_4$ and $CuFe_2O_4$, providing further evidence for the presence of $ZnFe_2O_4$ as a shell surrounding $CuFe_2O_4$[33].

### TEM and EDX spectrum

Figure 4 presents transmission electron microscopy (TEM) images depicting the $CuFe_2O_4$, $ZnFe_2O_4$ nanoparticles, and $CuFe_2O_4$/$ZnFe_2O_4$ core/shell. One can see that the shape and particle size distribution of the ferrite particles are uniform. As shown in Fig. 4, the histogram for bare ferrites and core/shell nanoparticles was used to determine the particle size distribution. The particle size was found to be approximately 9, 12 and 25 nm, with an error margin of 2 nm for $CuFe_2O_4$, $ZnFe_2O_4$, and $CuFe_2O_4$/$ZnFe_2O_4$, respectively. These values align well with the measurements obtained from X-ray diffraction (XRD). The uniform shell thickness is around 7 nm thick, while the core size is about 18 nm. However, particle agglomeration occurs as a result of magnetostatic interactions between particles or because nanoparticles experience a permanent magnetic moment proportionate to their volume.

Furthermore, Fig. 5 illustrates the quantitative EDX analysis conducted at different points and extensive regions to ascertain the elemental composition of the three samples. The results obtained after applying ZAF correction indicated that the atomic weight of the synthesized materials is consistent with the expected stoichiometric ratios. The presence of some Ca peaks in the EDX spectra of both bare ferrites may indicate the presence of small amounts (less than 2.4% by weight) of chemical impurities coming from the precursor materials. Therefore, the samples can be regarded as pure and in strong accordance with the XRD results. From Fig. 6, one can see that at the same point, the Cu and Zn elements, in core/shell sample, have weight percentages of 8.93, and 19.52, respectively, which were confirmed by the XRD refinement analysis. Such a result gives confidence to the formation of core/shell nanoparticles.

### FTIR

Figure 7 displays the Fourier transform infrared (FTIR) spectrum of the investigated samples to confirm the spinel ferrite phase formation and to ensure that there are no chemical residues inside the prepared nanoparticles. The spectrum is presented within the wave-number range of 400–4000 cm⁻¹. The infrared spectra of the compound exhibit two prominent absorption bands, namely $\upsilon_t$ which are observed at wavenumbers (≈ 560 to 565 cm⁻¹) assigned to the tetrahedral complexes and $\upsilon_o$ at wavenumbers (≈ 400 to 450 cm⁻¹) which associated with the vibrations of high valence cation(s) (such as $Fe^{3+}$–$O^{2-}$) that occupy the octahedral site[34]. The two vibration bands observed in this study are associated with the intrinsic vibrations occurring at the octahedral and tetrahedral sites within the spinel structure, respectively[34]. Both the strong wide band at 3420 cm⁻¹ and the weaker band at 1642 cm⁻¹ result from the interaction of O–H stretching vibrations with H bonds[35]. Furthermore, the peaks observed at wavenumbers 3427 cm⁻¹ and 1632 cm⁻¹ are attributed to bending and stretching vibrations of H–O–H which confirms the existence of absorbed water[2,17,19].

### Photoluminescence (PL) spectroscopy

Photoluminescence (PL) is used to study the electronic interaction at the surface between the core and shell structure. Figure 8 shows the PL emission spectra carried out at the excitation wavelength of 325 nm ($E_{exc.}$ = 3.8eV), which is greater than the energy gaps of Zn ferrite (2.1 eV)[28] and Cu ferrite (1.9 eV)[22,23]. One can see that the PL signal is very strong for Cu ferrite while it is very weak for Zn ferrite. This means that the recombination rate between electron–hole pairs is much faster for Cu ferrite than in Zn ferrite. On the other side, the PL signal for core/shell structure is slightly decreased; because of a generation of trapping states at the interface between the core and shell ferrites, as well as it was observed to exhibit a slight redshift, indicating a decrease in wavelength. This could be attributed to the quantum confinement effect[18,28]. The proposed electronic structure is shown in Fig. 9. The modification of PL signal for the core/shell structure could be useful for hydrogen production as well as for water purification as photocatalysis.

### Magnetic properties

Figure 10 shows the hysteresis loop for the investigated samples. One can see that, the Cu ferrite ($CuFe_2O_4$) sample has identical ferromagnetic behavior with fast saturation at magnetic field intensity $\geq$ 5000$G$.

Additionally, the magnetization data extracted from hysteresis loop were fitted employing the Law of approach to saturation (LAS) using the least squares approach, which is demonstrated by the following equation[2,29].
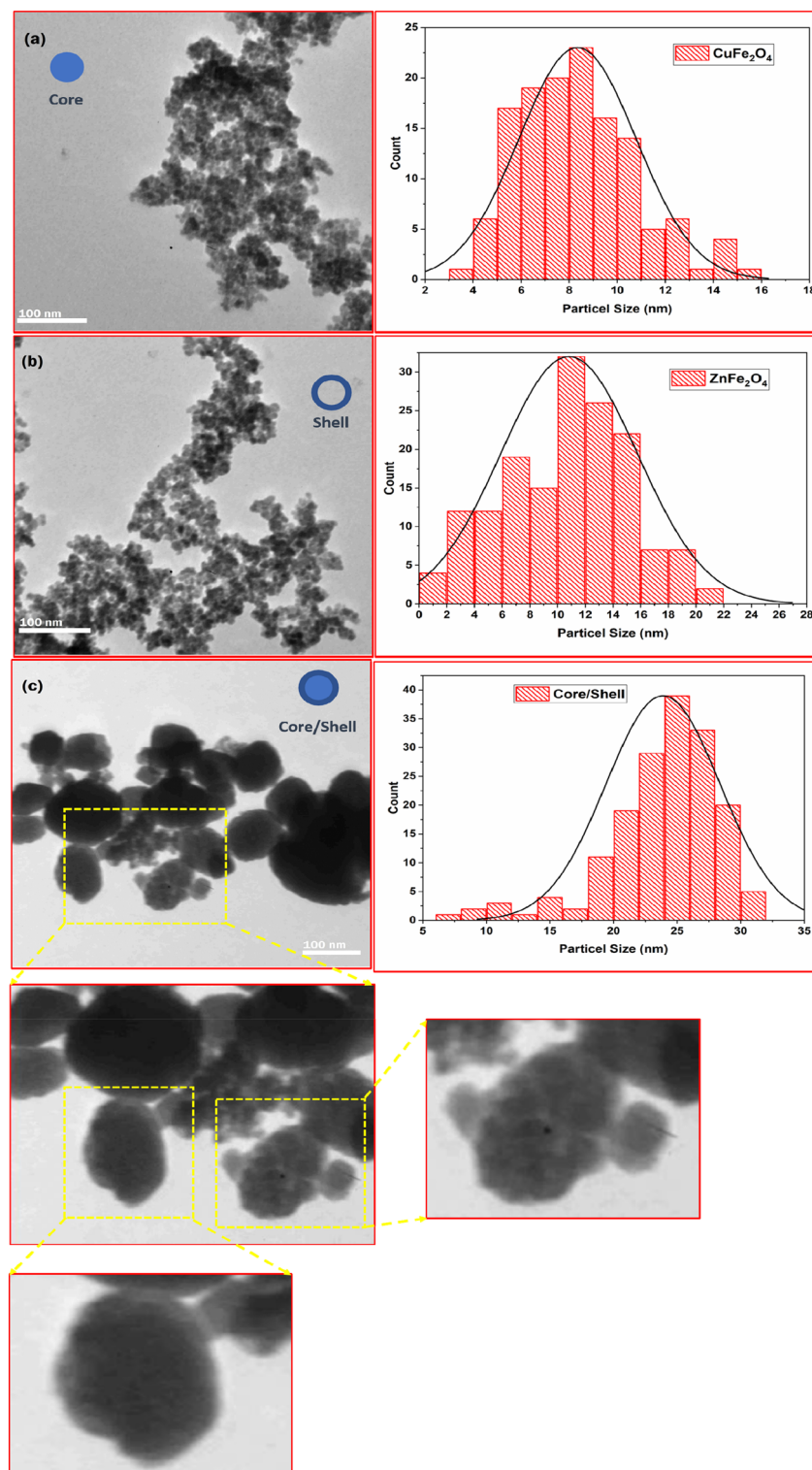
**Figure 4.** TEM images of (**a**) CuFe$_2$O$_4$, (**b**) ZnFe$_2$O$_4$ nanoparticles, and (**c**) CuFe$_2$O$_4$/ZnFe$_2$O$_4$ core/shell.

$$M = M_s \left( 1 - \frac{B}{H^2} \right) \tag{4}$$

The parameter (B) is induced by crystal anisotropy, which is related to the cubic anisotropy constant. The above equation describes the relation between the field (H) and (M) in the high field region as illustrated in Fig. 11a. The fitting curves (M vs. 1/H$^2$ data) for CuFe$_2$O$_4$, ZnFe$_2$O$_4$ and CuFe$_2$O$_4$/ZnFe$_2$O$_4$ core/shell nanoparticles are shown in Fig. 11b. The value of the obtained saturated magnetization (M$_s$) is about 7.6 emu/g (Table 1),
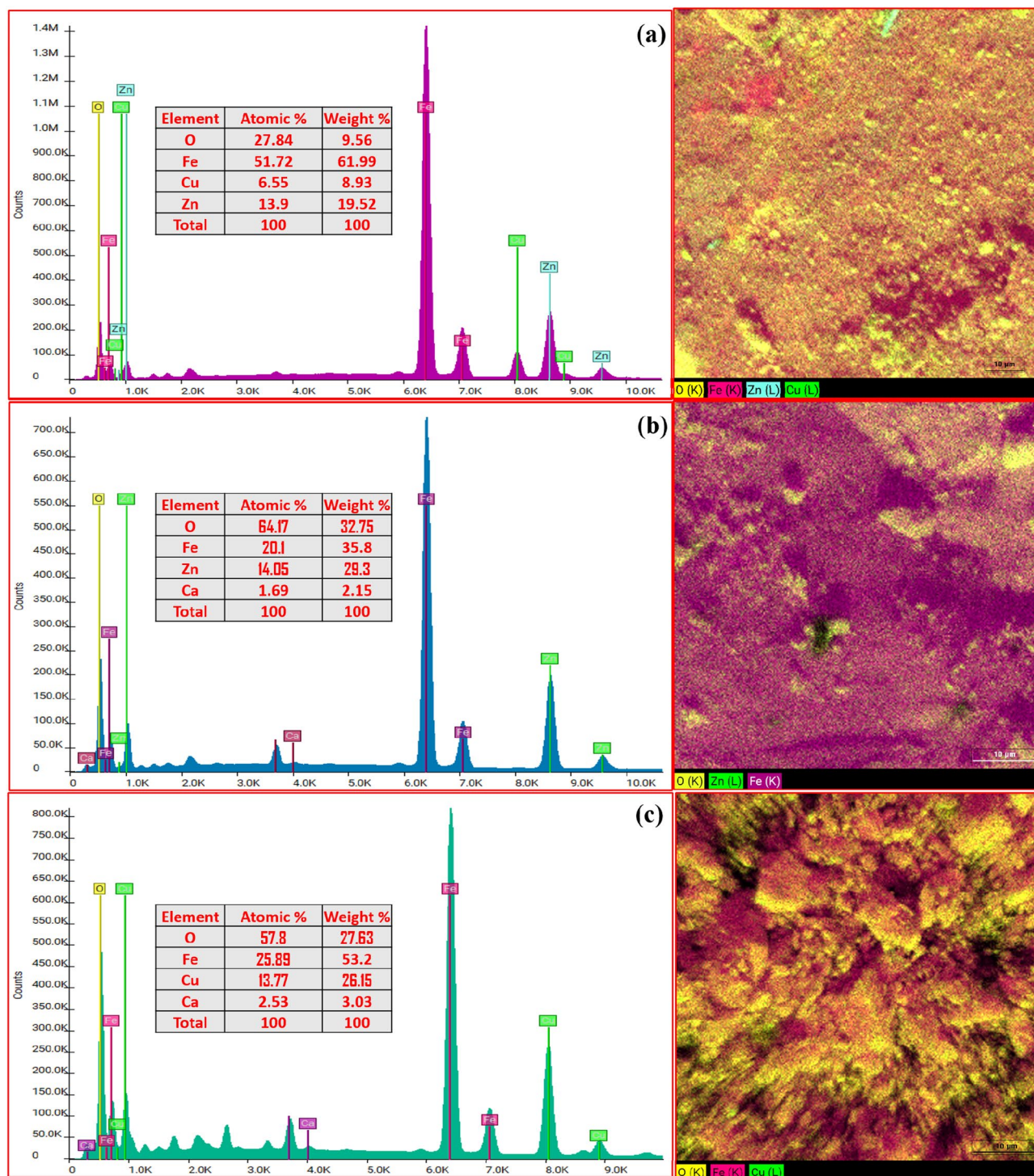
**Figure 5.** EDX spectra and Mapping of (**a**) $CuFe_2O_4/ZnFe_2O_4$ core/shell, (**b**) $ZnFe_2O_4$, and (**c**) $CuFe_2O_4$ nanoparticles.

which is lower than the $M_s$ value of bulk Cu ferrite ($\approx 60$ emu/g)[36–38]. This reduction could be explained by the presence of a magnetic dead layer as a result of a high surface-to-volume ratio due to the discontinuity of the magnetic moments at the surface of the nanoparticles and the presence of random canting of particle surface spins at the surface [39–41]. However, by comparing both values of saturated magnetization, the thickness of the dead layer (δ) could be calculated according to the following relations:

$$(M_s)_{nano}/(M_s)_{bulk} = r_{nano}^3/r_{bulk}^3 \text{ and } \delta_{\text{dead layer}} = r_{\text{size}} - r_{\text{eff}} \approx 7 \text{ nm} \quad (5)$$
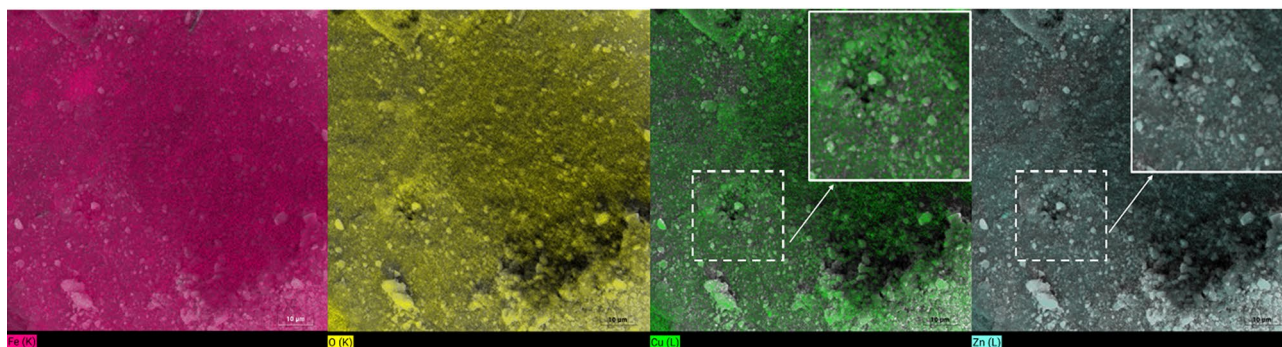
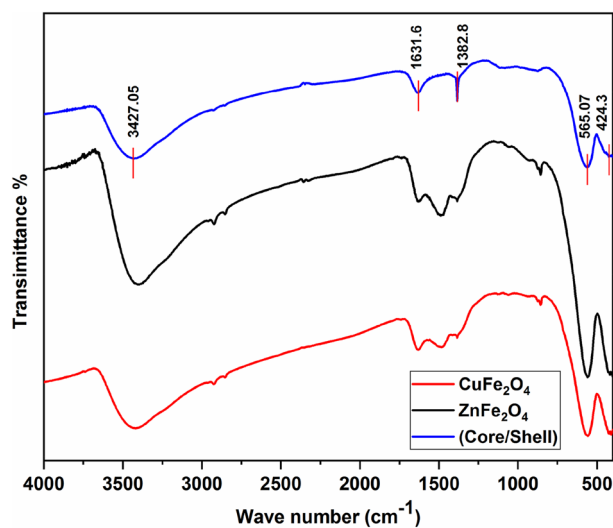**Figure 6.** Mapping images of $CuFe_2O_4/ZnFe_2O_4$ core/shell nanoparticles.



**Figure 7.** FTIR spectra of $CuFe_2O_4$, $ZnFe_2O_4$ and $CuFe_2O_4/ZnFe_2O_4$ core/shell nanoparticles.



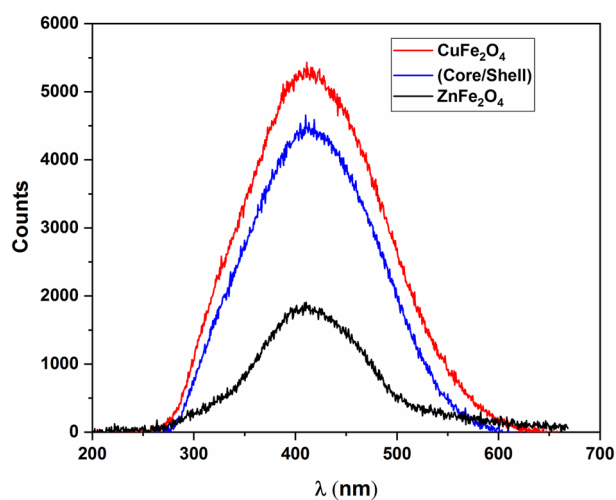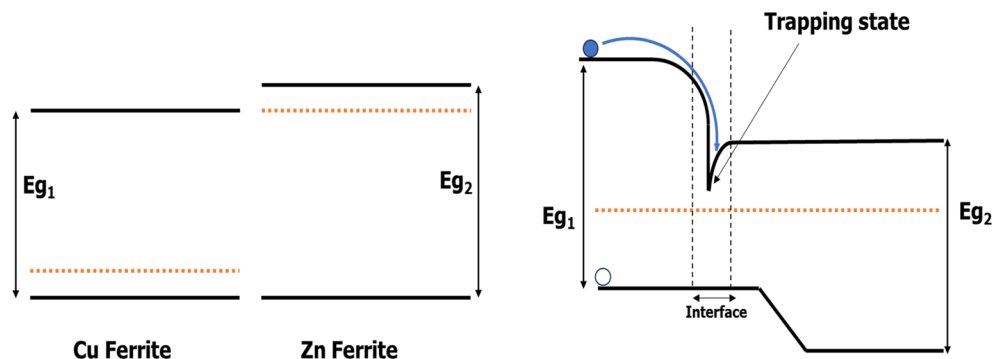**Figure 8.** PL spectra for $CuFe_2O_4$, $ZnFe_2O_4$ and $CuFe_2O_4/ZnFe_2O_4$ core/shell nanoparticles.

**Figure 9.** Schematic represents the band diagrams of both ferrites (left) and the trapping state occurs due to the interface between the core and shell (right).
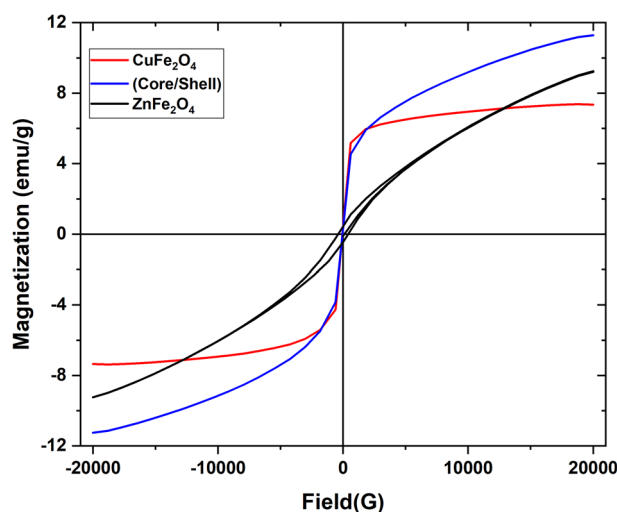


**Figure 10.** Magnetic hysteresis loop of $CuFe_2O_4$, $ZnFe_2O_4$ and $CuFe_2O_4/ZnFe_2O_4$ core/shell nanoparticles.

The Zn ferrites sample exhibits superparamagnetic behavior, and by Langevin function fitting[42,43], $M_s$ was found to be around 10 emu/g which is in agreement with the bulk saturated magnetization value[44,45], which means there is no magnetic dead layer due to the antiferromagnetic behavior of Zn ferrite. On the other hand, for the $CuFe_2O_4/ZnFe_2O_4$ core/shell nanostructure, the saturated magnetization $M_s$ increased dramatically up to 12.4 emu/g, which is an interesting behavior. This increasing behavior is not simply a linear combination of the magnetization values of both Cu ferrite and Zn ferrite. Alternately, it can be represented as follows:

$$M_s(core/shell) = 0.33\, M_s(ZnFe_2O_4) + 0.67\, M_s(CuFe_2O_4) + M_s(Cu/Zn) \tag{6}$$

The last term in the above equation is the increase in magnetization due to the interfacial effects between the core and shell. Substituting the experimental values of $M_s$ in the above equation, we get:

$$(12.4\text{ emu/g}) = (0.33)(10\text{ emu/g}) + (0.67)(7.6\text{ emu/g}) + M_s(Cu/Zn) \tag{7}$$

Then, the value of $M_s(Cu/Zn) = 4.01$ emu/g. The enhancement of the magnetization could be explained in terms of the decrease in thickness of the magnetic dead layer due to the continuity of the interaction at the surface of core Cu ferrite and Zn ferrite as a shell. Furthermore, in deep sight, the hysteresis loop of the core/shell sample displays the failure to reach magnetic saturation. This behavior could be explained in terms of the presence of $Fe_2O_3$ as a weakly ferromagnetic or antiferromagnetic phase that initiates the superparamagnetic tendency, i.e., it resists the magnetic moment rotation due to the limited response of the antiferromagnetic moments to the applied field[46], as well as, it suggests some degree of non-collinear spin structure, which is normally described by a core/shell particle model[47]. It's valuable to note that the core/shell sample also has superparamagnetic behavior (i.e., $H_c = 0$).

## Magnetic loss (heating ability of the samples)

One of the most important studies is the magnetic losses of the material at high frequency. The magnetic loss or heating ability is determined by measuring the increase in temperature over time for the three samples.
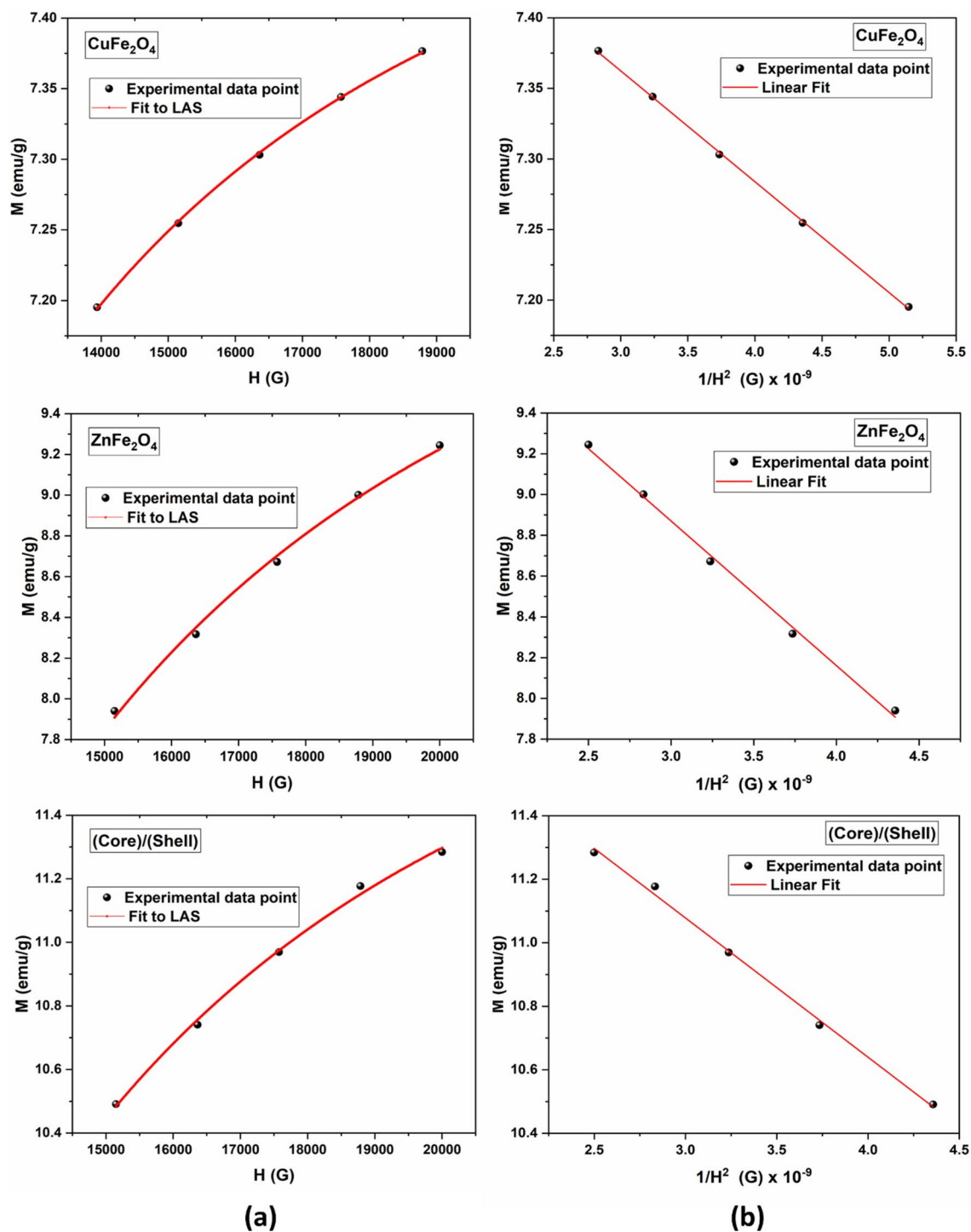
**Figure 11.** (**a**) 'Law of approach' fit to M versus H, and (**b**) linear fit of M versus $1/H^2$ for $CuFe_2O_4$, $ZnFe_2O_4$ and $CuFe_2O_4/ZnFe_2O_4$ core/shell nanoparticles.

The design and operation of the used induction heating circuit are described in detail elsewhere[48,49]. Figure 12 depicts the rise in temperature of the investigated samples with time within for an exposure duration of 10 min. It is evident that the Cu ferrite sample has the maximum magnetic loss (the slope of T vs. time) while the Zn ferrite, as expected because of its antiferromagnetic behavior, has the least loss. Typically, hysteresis loss, eddy loss, Néel relaxation, and the Brownian rotation all contribute to the magnetic loss in samples of multi-domain magnetic NPs[29,50]. The generation of hysteresis loss can be attributed to the movements and rotations of magnetic domain walls[51]. When a material undergoes sinusoidal magnetization, the voltage induced within the material exhibits an opposite polarity compared to the voltages responsible for generating the magnetizing current and the alternating magnetic field. Consequently, circular currents are induced, which give rise to magnetic fields that are oriented in the opposite direction to that of the initial current. The eddy current exhibits its maximum
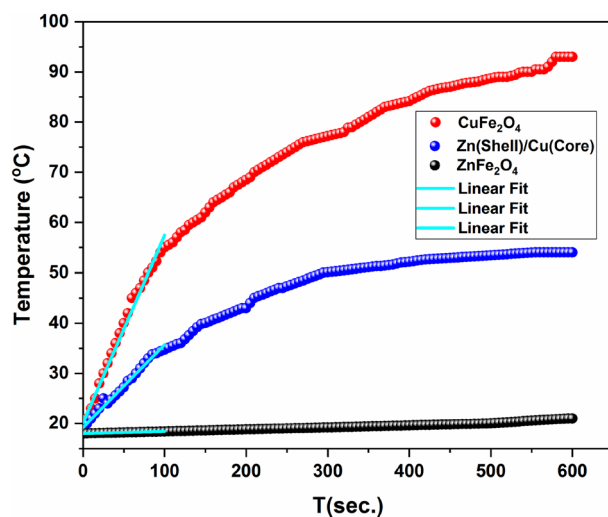
**Figure 12.** Temperature rise with time for $CuFe_2O_4$, $ZnFe_2O_4$ and $CuFe_2O_4$/$ZnFe_2O_4$ core/shell nanoparticles.

strength at the core of the magnetic material particle. Moreover, it is worth noting that hysteresis loss is primarily observed in particles with large crystallites and multiple domains, whereas relaxation loss is observed in particles with a single domain[52]. However, it has been established that the hysteresis and eddy current heating effects can be ignored when dealing with particles with sizes smaller than 20 nm[29]. On the other hand, Néel and Brownian relaxations cause magnetic loss in superparamagnetic materials (i.e., $H_c = 0$). As the sample is in powder form, Brownian relaxation is ruled out because it occurs by particle rotation in the carrier liquid. Hence, for the Cu ferrite sample, we suggested that the primary mechanism responsible magnetic loss is the Néel relaxation[53,54].

The temperature of the powder samples ($CuFe_2O_4$ and core/shell) increased initially and ultimately reached a state of saturation. The measurement of the heat ability of the samples ($\Delta T/\Delta t$) is obtained by calculating the slope from the linear segment as shown in Fig. 12. It is valuable to notice that the magnetic loss of core/shell structure decreased in comparison to the bare $CuFe_2O_4$ although its magnetization increased. This property renders the core/shell structure very useful in high frequencies applications. The high magnetization value of the core/shell sample is not reflected on its heating ability. The presence of the $Fe_2O_3$ phase, as previously mentioned in relation to hysteresis measurements, reduces the magnetic loss (the samples' heating ability) by obstructing the rotation of magnetic moments in response to an external magnetic field[55]. This, in turn, reduces the Néel rotation in response to a high-frequency field.

## Conclusions

Core/shell magnetic nanoparticles were synthesized using hydrothermal technique. The mechanism of core/shell formation is determined by the lattice matching between both $CuFe_2O_4$ and $ZnFe_2O_4$ nanoparticles. Moreover, the PL signal of core/shell nanoparticles was found to be between bare ferrites; $CuFe_2O_4$ and $ZnFe_2O_4$. Like change of the PL signal for the core/shell structure compared to both pure ferrite nanoparticles could be advantageous for the creation of hydrogen as well as for the photocatalytic purification of water. The Law of approach to saturation (LAS) was used to deduce the accurate magnetization values for the investigated samples. The magnetization of the core/shell nanocomposite was found to be approximately 63% higher than that of pure Cu ferrite, while the magnetic loss decreased. It is important to acknowledge that the core/shell sample exhibits superparamagnetic behavior. This property holds great promise for various applications.

## Data availability

The data that support the findings of this study are available from the corresponding author upon request.

## References

1. Baykal, A. *et al.* Magnetic properties and hyperfine interactions of $Co_{1-2x}Ni_xMnxFe_2O_4$ nanoparticles. *Ceram. Int.* **43**, 4746–4752 (2017).
2. Faramawy, A. M., Elsayed, H. & Agami, W. R. Correlation between structure, cation distribution, elastic, and magnetic properties for $Bi^{3+}$ substituted Mn–Zn ferrite nanoparticles. *Mater. Chem. Phys.* **314**, 128939 (2024).
3. Amir, M., Baykal, A., Güner, S., Güngüneş, H. & Sözeri, H. Magneto-optical investigation and hyperfine interactions of copper substituted $Fe_3O_4$ nanoparticles. *Ceram. Int.* **42**, 5650–5658 (2016).
4. Güner, S. *et al.* Synthesis and characterization of oleylamine capped $Mn_xFe_{1-x}Fe_2O_4$ nanocomposite: Magneto-optical properties, cation distribution and hyperfine interactions. *J. Alloys Compd.* **688**, 675–686 (2016).
5. Kahil, H., Faramawy, A., El-Sayed, H. & Abdel-Sattar, A. Magnetic properties and sar for gadolinium-doped iron oxide nanoparticles prepared by hydrothermal method. *Crystals* **11**, 1153 (2021).

6. Faramawy, A. M. *et al.* Unveiling the effect of Gd$^{3+}$ doping on enriching the structural, magnetic, optical, and dielectric properties of biocompatible hematite nanoparticles. *J. Alloys Compd.* **974**, 172845 (2024).

7. Xiao, N. *et al.* T1–T2 dual-modal MRI of brain gliomas using PEGylated Gd-doped iron oxide nanoparticles. *J. Colloid Interface Sci.* **417**, 159–165 (2014).

8. Gavrilov-Isaac, V. *et al.* Synthesis of trimagnetic multishell MnFe$_2$O$_4$@CoFe$_2$O$_4$@NiFe$_2$O$_4$ nanoparticles. *Small* **11**, 2614–2618 (2015).

9. Wei, S. *et al.* Multifunctional composite core–shell nanoparticles. *Nanoscale* **3**, 4474 (2011).

10. Sanna Angotzi, M. *et al.* Spinel ferrite core-shell nanostructures by a versatile solvothermal seed-mediated growth approach and study of their nanointerfaces. *ACS Nano* **11**, 7889–7900 (2017).

11. Morrison, S. A., Cahill, C. L., Carpenter, E. E., Calvin, S. & Harris, V. G. Atomic engineering of mixed ferrite and core-shell nanoparticles. *J. Nanosci. Nanotechnol.* **5**, 1323–1344 (2005).

12. Gabal, M. A., Al-Juaid, A. A., El-Rashed, S., Hussein, M. A. & Al-Angari, Y. M. Polyaniline/Co$_{0.6}$Zn$_{0.4}$Fe$_2$O$_4$ core-shell nanocomposites: Synthesis, characterization and properties. *J. Alloys Compd.* **747**, 83–90 (2018).

13. Record, P. *et al.* Direct and converse magnetoelectric effect in laminate bonded Terfenol-D-PZT composites. *Sens. Actuat. B Chem.* **126**, 344–349 (2007).

14. Mrotek, E. *et al.* Improved degradation of etodolac in the presence of core-shell ZnFe$_2$O$_4$/SiO$_2$/TiO$_2$ magnetic photocatalyst. *Sci. Total Environ.* **724**, 138167 (2020).

15. Shao, R., Sun, L., Tang, L. & Zhidong, C. Preparation and characterization of magnetic core–shell ZnFe2O4@ZnO nanoparticles and their application for the photodegradation of methylene blue. *Chem. Eng. J.* **217**, 185–191 (2013).

16. Tatarchuk, T. *et al.* Structural, Optical, and Magnetic Properties of Zn-Doped CoFe$_2$O$_4$ Nanoparticles. *Nanoscale Res. Lett.* **12**, (2017).

17. Taneja, S., Thakur, P., Ravelo, B. & Thakur, A. Nanocrystalline samarium doped nickel-zinc-bismuth ferrites: Investigation of structural, electrical and dielectric properties. *Mater. Res. Bull.* **154**, 111937 (2022).

18. Tatarchuk, T. R. *et al.* Effect of cobalt substitution on structural, elastic, magnetic and optical properties of zinc ferrite nanoparticles. *J. Alloys Compd.* **731**, 1256–1266 (2018).

19. Sundararajan, M., John-Kennedy, L. & Judith-Vijaya, J. Synthesis and characterization of cobalt substituted zinc ferrite nanoparticles by microwave combustion method. *J. Nanosci. Nanotechnol.* **15**, 6719–6728 (2015).

20. Chung, P. H. *et al.* A sensitive visible light photodetector using cobalt-doped zinc ferrite oxide thin films. *ACS Appl. Mater. Interfaces* **13**, 6411–6420 (2021).

21. Shao, R., Sun, L., Tang, L. & Zhidong, C. Preparation and characterization of magnetic core-shell ZnFe$_2$O$_4$@ZnO nanoparticles and their application for the photodegradation of methylene blue. *Chem. Eng. J.* **217**, 185–191 (2013).

22. Park, S. *et al.* Rapid flame-annealed CuFe$_2$O$_4$ as efficient photocathode for photoelectrochemical hydrogen production. *ACS Sustain. Chem. Eng.* **7**, 5867–5874 (2019).

23. Liu, Y. *et al.* Insights into the interfacial carrier behaviour of copper ferrite (CuFe$_2$O$_4$) photoanodes for solar water oxidation. *J. Mater. Chem. A* **7**, 1669–1677 (2019).

24. Tran Thi, T. U. *et al.* Synthesis of magnetic CuFe$_2$O$_4$/Fe$_2$O$_3$ core-shell materials and their application in photo-Fenton-like process with oxalic acid as a radical-producing source. *J. Asian Ceram. Soc.* **9**, 1091–1102 (2021).

25. Balaji, M., Chithra Lekha, P. & Pathinettam Padiyan, D. Core-shell structure in copper ferrite-polyaniline nanocomposite: Confirmation by laser Raman spectra. *Vib. Spectrosc.* **62**, 92–97 (2012).

26. Kuo, S. H. *et al.* Fabrication of anisotropic Cu ferrite-polymer coreshell nanoparticles for photodynamic ablation of cervical cancer cells. *Nanomaterials* **10**, 1–19 (2020).

27. Mulud, F. H., Dahham, N. A. & Waheed, I. F. Synthesis and characterization of copper ferrite nanoparticles. *IOP Conf. Ser. Mater. Sci. Eng.* **928**, 072125 (2020).

28. Manikandan, A., Kennedy, L. J., Bououdina, M. & Vijaya, J. J. Synthesis, optical and magnetic properties of pure and Co-doped ZnFe$_2$O$_4$ nanoparticles by microwave combustion method. *J. Magn. Magn. Mater.* **349**, 249–258 (2014).

29. Faramawy, A. M., Mattei, G., Scian, C., Elsayed, H. & Ismail, M. I. M. Cr$^{3+}$ substituted aluminum cobalt ferrite nanoparticles: Influence of cation distribution on structural and magnetic properties. *Phys. Scr.* **96**, 125849 (2021).

30. Kant, R., Kumar, D. & Dutta, V. High coercivity α-Fe$_2$O$_3$ nanoparticles prepared by continuous spray pyrolysis. *RSC Adv.* **5**, 52945–52951 (2015).

31. Lutterotti, L., Gualtieri, A. & Aldrighetti, S. Rietveld refinement using Debye-Scherrer film techniques. *Mater. Sci. Forum* **228–231**, 29–34 (1996).

32. Williamson, G. K. & Hall, W. H. X-ray line broadening from filed aluminium and wolfram. *Acta Metall.* **1**, 22–31 (1953).

33. Sattar, A. A., El-Sayed, H. M. & Alsuqia, I. Structural and magnetic properties of CoFe$_2$O$_4$/NiFe$_2$O$_4$ core/shell nanocomposite prepared by the hydrothermal method. *J. Magn. Magn. Mater.* **395**, 89–96 (2015).

34. Agami, W. R. Composition and temperature dependence of the dielectric properties of (Silicone Rubber/CoZn nanoferrite) composites. *Appl. Phys. A Mater. Sci. Process.* **127**, 1–11 (2021).

35. Sathishkumar, G., Venkataraju, C., Murugaraj, R. & Sivakumar, K. Bismuth effect in the structural, magnetic and dielectric properties of CoZn ferrite. *J. Mater. Sci. Mater. Electron.* **23**, 243–250 (2012).

36. Rashad, M. M., Mohamed, R. M., Ibrahim, M. A., Ismail, L. F. M. & Abdel-Aal, E. A. Magnetic and catalytic properties of cubic copper ferrite nanopowders synthesized from secondary resources. *Adv. Powder Technol.* **23**, 315–323 (2012).

37. Goya, G. F., Rechenberg, H. R. & Jiang, J. Z. Structural and magnetic properties of ball milled copper ferrite. *J. Appl. Phys.* **84**, 1101–1108 (1998).

38. Marinca, T. F., Chicinaş, I. & Isnard, O. Structural and magnetic properties of the copper ferrite obtained by reactive milling and heat treatment. *Ceram. Int.* **39**, 4179–4186 (2013).

39. Muhammad, A., Sattar, A. A., Elsayed, H. M. & Ghani, A. A. Microstructure, magnetic, optical and catalytic activity of Li–Co–Cd nanoferrites. *J. Mater. Sci. Mater. Electron.* **29**, 3856–3866 (2018).

40. Mallesh, S. & Srinivas, V. A comprehensive study on thermal stability and magnetic properties of MnZn-ferrite nanoparticles. *J. Magn. Magn. Mater.* **475**, 290–303 (2019).

41. Gul, I. H., Maqsood, A., Naeem, M. & Ashiq, M. N. Optical, magnetic and electrical investigation of cobalt ferrite nanoparticles synthesized by co-precipitation route. *J. Alloys Compd.* **507**, 201–206 (2010).

42. Faramawy, A., Elsayed, H., Scian, C. & Mattei, G. Structural, optical, magnetic and electrical properties of sputtered ZnO and ZnO: Fe thin films: the role of deposition power. *Ceramics* **5**, 1128–1153 (2022).

43. Moumen, N. & Pileni, M. P. Control of the size of cobalt ferrite magnetic fluid. *J. Phys. Chem.* **100**, 1867–1873 (1996).

44. Xu, Y. *et al.* Preparation and magnetic properties of ZnFe$_2$O$_4$ nanotubes. *J. Nanomater.* **2011**, 1–6 (2011).

45. Bohra, M. *et al.* Competing magnetic interactions in inverted Zn-ferrite thin films. *Magnetism* **2**, 168–178 (2022).

46. Iacovita, C. *et al.* Polyethylene glycol-mediated synthesis of cubic iron oxide nanoparticles with high heating power. *Nanoscale Res. Lett.* https://doi.org/10.1186/s11671-015-1091-0 (2015).

47. Raghavender, A. T. *et al.* Synthesis and magnetic properties of NiFe$_{2-x}$Al$_x$O$_4$ nanoparticles. *J. Magn. Magn. Mater.* **316**, 1–7 (2007).

48. Kahil, H. & El-Sayed, H. M. Assessment of AC losses in cobalt ferrite nanoparticles using a varying frequency induction heater. *IOSR J. Appl. Phys.* **7**, 37–43 (2015).

49. Sattar, A. A., Elsayed, H. M. & Faramawy, A. M. Comparative study of structure and magnetic properties of micro- and nano-sized Gd$_x$Y$_{3-x}$Fe$_5$O$_{12}$ garnet. *J. Magn. Magn. Mater.* **412**, 172–180 (2016).

50. Vallejo-Fernandez, G. *et al.* Mechanisms of hyperthermia in magnetic nanoparticles. *J. Phys. D. Appl. Phys.* **46**, 312001 (2013).

51. Wildeboer, R. R., Southern, P. & Pankhurst, Q. A. On the reliable measurement of specific absorption rates and intrinsic loss parameters in magnetic hyperthermia materials. *J. Phys. D. Appl. Phys.* **47**, 495003 (2014).

52. Motoyama, J. *et al.* Hyperthermic treatment of DMBA-induced rat mammary cancer using magnetic nanoparticles. *Biomagn. Res. Technol.* **6**, 1–6 (2008).

53. Hergt, R., Dutz, S. & Zeisberger, M. Validity limits of the Néel relaxation model of magnetic nanoparticles for hyperthermia. *Nanotechnology* **21**, 015706 (2010).

54. Kötitz, R., Weitschies, W., Trahms, L. & Semmler, W. Investigation of Brownian and Néel relaxation in magnetic fluids. *J. Magn. Magn. Mater.* **201**, 102–104 (1999).

55. Lemine, O. M., Madkhali, N., Hjiri, M., All, N. A. & Aida, M. S. Comparative heating efficiency of hematite ($\alpha$-Fe$_2$O$_3$) and nickel ferrite nanoparticles for magnetic hyperthermia application. *Ceram. Int.* **46**, 28821–28827 (2020).

## Author contributions

A.M.F. and H.M.E.-S. handling the experimental work, analyzed the data, wrote and editing the manuscript.

## Funding

## Competing interests

The authors declare no competing interests.

## Additional information

**Correspondence** and requests for materials should be addressed to A.M.F.

**Reprints and permissions information** is available at www.nature.com/reprints.

**Publisher's note** Springer Nature remains neutral with regard to jurisdictional claims in published maps and institutional affiliations.